2000

Computational Simulation of Dynamic Stall on the NLR 7301 Airfoil

Weber, S.

Academic Press

Journal of Fluids and Structures (2000) 14, 779-798
http://hdl.handle.net/10945/50286

Journal of Fluids and Structures (2000) **14,** 779–798
doi:10.1006/jfls.2000.0299, available online at http://www.idealibrary.com on IDEAL®

COMPUTATIONAL SIMULATION OF DYNAMIC STALL ON THE NLR 7301 AIRFOIL

S. Weber† and M. F. Platzer

Department of Aeronautics and Astronautics, Naval Postgraduate School Monterey, CA 93943-5000, U.S.A.

(Received 28 February 1999, and in final form 20 March 2000)

The dynamic stall behavior of the supercritical NLR 7301 airfoil is analyzed with a 2-D thin-layer Navier–Stokes code. The code solves the compressible Reynolds-averaged Navier-Stokes equations with an upwind biased numerical scheme in combination with the Baldwin–Lomax or the Baldwin–Barth turbulence models. The effect of boundary layer transition is incorporated using the transition length model of Gostelow *et al.* The transition onset location is determined with Michel's formula or it can be specified as an input parameter. The two turbulence models yield significantly different steady-state lift coefficients at incidences greater than 8°. The use of the one-equation Baldwin–Barth model together with the Gostelow transition model is found to give substantially better agreement with the experimental data of McCroskey *et al.* than the Baldwin–Lomax model. Also, the unsteady computations are strongly affected by the choice of the turbulence model. The Baldwin–Barth model predicts the lift hysteresis loops consistently better than the algebraic turbulence model. However, the one-equation model improves the prediction of the moment hysteresis loops only for one test case.

1. INTRODUCTION

Dynamic stall limits the helicopter flight envelope and methods are required to predict its occurrence. Dynamic stall also occurs on wind turbines, propellers, and turbomachinery blades. At present, dynamic stall prediction method used by the helicopter, turbomachinery, aircraft, and wind turbine industries are largely based on semi-empirical approaches. The very complex dynamic stall phenomena which have recently been reviewed by Carr & Chandrasekhara (1996) greatly impede the development of nonempirical prediction methods. Nevertheless, recent progress in the numerical analysis of dynamic stall phenomena, as summarized by Ekaterinaris & Platzer (1997), suggests the possibility of developing prediction methods which are based on the solution of the viscous flow equations.

The present paper is a continuation of systematic studies begun by Ekaterinaris *et al.* (1995), Ekaterinaris & Platzer (1996) and Sanz & Platzer (1998) to explore the feasibility of computing stall onset and dynamic stall using the Navier–Stokes equations in combination with advanced turbulence and transition models. Encouraging results were obtained for the NACA 0012 and Sikorsky SC 1095 airfoils. It is the objective of the present paper to report similar computations for the NLR 7301 airfoil. This airfoil was chosen for the study because detailed experimental data are available from McCroskey *et al.* (1982) and Schewe & Deyhle (1996).

†DaimlerChrysler Aerospace, MTU München, Munich, Germany.

0889–9746/00/080779 + 20 $35.00/0

2. NUMERICAL METHOD

The unsteady, nonlinear and compressible Navier–Stokes algorithm solves the strong conservation-law form of the two-dimensional, thin-layer Navier–Stokes equations in a curvilinear coordinate system (ξ, η). The governing equations are given in vector form by

$$\partial_t \hat{\mathbf{Q}} + \partial_\xi \hat{\mathbf{E}} + \partial_\eta \hat{\mathbf{F}} = \mathrm{Re}^{-1} \partial_\eta \hat{\mathbf{S}}, \tag{1}$$

where $\hat{\mathbf{Q}}$ is the vector of conservative variables

$$\hat{\mathbf{Q}} = \frac{1}{J} \begin{Bmatrix} \rho \\ \rho u \\ \rho v \\ e \end{Bmatrix}, \tag{2}$$

$\hat{\mathbf{E}}$ and $\hat{\mathbf{F}}$ are the inviscid flux vectors

$$\hat{\mathbf{E}} = \frac{1}{J} \begin{Bmatrix} \rho U \\ \rho u U + \xi_x p \\ \rho v U + \xi_y p \\ (e + p) U - \xi_t p \end{Bmatrix}, \quad \hat{\mathbf{F}} = \frac{1}{J} \begin{Bmatrix} \rho V \\ \rho u V + \eta_x p \\ \rho v V + \eta_y p \\ (e + p) V - \eta_t p \end{Bmatrix}, \tag{3}$$

and $\hat{\mathbf{S}}$ is the thin-layer approximation of the viscous fluxes in the η direction (normal to the airfoil surface),

$$\hat{\mathbf{S}} = \frac{1}{J} \begin{Bmatrix} 0 \\ \mu m_1 u_\eta + (\mu/3) m_2 \eta_x \\ \mu m_1 v_\eta + (\mu/3) m_2 \eta_y \\ \mu m_1 m_3 + (\mu/3) m_2 m_4 \end{Bmatrix}, \tag{4}$$

in which

$$m_1 = \eta_x^2 + \eta_y^2, \tag{5}$$

$$m_2 = \eta_x u_\eta + \eta_y v_\eta, \tag{6}$$

$$m_3 = (u^2 + v^2)/2 + (\kappa - 1)^{-1} \mathrm{Pr}^{-1} \partial_\eta (a^2), \tag{7}$$

$$m_4 = \eta_x u + \eta_y v. \tag{8}$$

The terms U and V are the contravariant velocity components given by

$$U = u\xi_x + v\xi_y + \xi_t, \quad V = u\eta_x + v\eta_y + \eta_t, \tag{9}$$

and J is the metric Jacobian, where

$$J^{-1} = x_\xi y_\eta - x_\eta y_\xi. \tag{10}$$

Pressure is related to the other variables through the equation of state for an ideal gas:

$$p = (\kappa - 1)[e - \rho(u^2 + v^2)/2]. \tag{11}$$

Equations (1–11) are nondimensionalized using c as the reference length, a_∞ as the reference velocity, c/a_∞ as the reference time, ρ_∞ as the reference density and $\rho_\infty a_\infty^2$ as the reference energy.

For Euler solutions, the viscous terms on the right-hand side are set to zero, and flow tangency boundary conditions are applied at the surface. For Navier–Stokes solutions the

no-slip condition is applied. Density and pressure are extrapolated to the surface for both Euler and Navier–Stokes solutions. For unsteady motions, the flow-tangency and no-slip conditions are modified to include the local motion of the surface which also contributes to the pressure on the surface. Therefore, the momentum equation normal to the surface (η direction) is solved to predict the pressure for a viscous flow more accurately:

$$\partial_\eta p|_{\text{wall}} = -\frac{1}{\nabla^2 \eta}\left[\rho \partial_t \begin{Bmatrix} \dot{x}|_{\text{wall}} \\ \dot{y}|_{\text{wall}} \end{Bmatrix} \cdot \nabla\eta + \partial_\eta p|_{\text{wall}} \nabla\xi \cdot \nabla\eta\right], \tag{12}$$

where $\dot{x}|_{\text{wall}}$ and $\dot{y}|_{\text{wall}}$ are the components of the blade velocity. Furthermore, it is assumed that the grid is orthogonal at the surface, and therefore $\nabla\xi \cdot \nabla\eta = 0$. If the blade does not move, the normal pressure gradient is equal to zero according to boundary layer theory.

The time integration is performed using the third-order upwind biased, factorized, iterative, implicit scheme of Rai & Chakravarthy (1988) tested by Ekaterinaris & Platzer (1996) and given by

$$\begin{aligned}[I + h_\xi(\nabla_\xi \hat{A}^+_{i,k} + \Delta_\xi \hat{A}^-_{i,k})]^p \times [I + h_\eta(\nabla_\eta \hat{B}^+_{i,k} + \Delta_\eta \hat{B}^-_{i,k} - \mathrm{Re}^{-1}\delta_\eta \hat{M}_{i,k})]^p \\ \times (\hat{Q}^{p+1}_{i,k} - \hat{Q}^p_{i,k}) = -[(\hat{Q}^p_{i,k} - \hat{Q}^n_{i,k}) + h_\xi(\hat{E}^p_{i+1/2,k} - \hat{E}^p_{i-1/2,k}) \\ + h_\eta(\hat{F}^p_{i,k+1/2} - \hat{F}^p_{i,k-1/2}) - \mathrm{Re}^{-1} h_\eta(\hat{S}^p_{i,k+1/2} - \hat{S}^p_{i,k-1/2})] \,.\end{aligned} \tag{13}$$

In equation (13), $h_\xi = \Delta t/\Delta\xi$, etc., $\hat{A}^\pm = \partial\hat{E}/\partial\hat{Q}$, etc., are the flux Jacobian matrices and ∇, Δ and δ are the forward, backward and central difference operators, respectively. The quantities $\hat{E}_{i+1/2,k}$, $\hat{F}_{i,k+1/2}$ and $\hat{S}_{i,k+1/2}$ are numerical fluxes. The superscript $()^n$ denotes the time step, and the superscript $()^p$ refers to Newton subiterations within each time step. The inviscid fluxes, $\hat{E}$ and $\hat{F}$, are evaluated using Osher's third-order upwinding scheme (Chakravarthy & Osher 1985). For the linearization of the left-hand side of equation (13) the flux Jacobian matrices, A and B, are evaluated by the Steger–Warming flux-vector splitting (Steger & Warming 1981). The viscous fluxes are computed with second-order central differences. Time accuracy is improved by performing Newton subiterations to convergence at each step. These subiterations minimize the linearization and factorization errors and help drive the left-hand side of equation (13) to zero at each time step. The present authors found that larger CFL numbers (i.e. a larger time step) could be used if the number of Newton iterations was increased. The optimum seemed to depend on the grid topology and flow conditions, but the best computational performance seemed to occur with 2–3 sub-iterations for Navier–Stokes simulations. The Navier–Stokes solver has been tested extensively in a variety of unsteady subsonic and transonic studies, such as Clarkson *et al.* (1993), Grohsmeyer *et al.* (1991), Ekaterinaris *et al.* (1994), and Ekaterinaris & Platzer (1996).

The turbulence modeling is based either on the standard algebraic model of Baldwin & Lomax (1978) or the one equation models of Baldwin & Barth (1990). The eddy viscosity obtained from the models is used for the computation of the fully turbulent region and for the evaluation of an effective eddy viscosity in the transitional flow region as is explained next.

3. TRANSITION MODELING

The transition modeling for all turbulence models follows Sanz & Platzer (1998). In this publication, the model of Gostelow *et al.* (1996) was introduced, which permits the

calculation of the transition length as a function of pressure gradient and free-stream turbulence level. This method continuously adjusts the turbulent spot growth in response to changes of the local pressure gradient.

The intermittency function in the transitional region is given by

$$\gamma(x) = 1 - \exp\left[- n \int_{x_t}^{x_i} \frac{\sigma}{\tan \varepsilon} \left(\frac{\mathrm{d}x}{U} \right) \int_{x_t}^{x_i} \tan \varepsilon \, \mathrm{d}x \right], \tag{14}$$

where the correlations for the variation of the spot propagation parameter σ and the spot spreading half-angle ε as functions of the pressure gradient parameter λ_θ are

$$\varepsilon = 4 + \frac{22{\cdot}14}{0{\cdot}79 + 2{\cdot}72 \exp(47{\cdot}63\lambda_\theta)} \tag{15}$$

and

$$\sigma = 0{\cdot}03 + \frac{0{\cdot}37}{0{\cdot}48 + 3{\cdot}0 \exp(52{\cdot}9\lambda_\theta)}. \tag{16}$$

Here $\lambda_\theta = (\theta^2/\nu)/(\mathrm{d}U/\mathrm{d}x)$ with the boundary-layer momentum thickness, θ, and the outer-edge velocity, U. The spot generation rate, n, is inferred from the dimensionless breakdown-rate parameter, N, where

$$N = n\sigma\lambda_{\theta_t}^3/\nu, \tag{17}$$

$$N = 0{\cdot}86^{-3} \exp[2{\cdot}134\lambda_{\theta_t} \ln(q_t) - 59{\cdot}23\lambda_{\theta_t} - 0{\cdot}564 \ln(q_t)], \quad \text{for } \lambda_{\theta_t} \leq 0 \tag{18}$$

and

$$N = N(\lambda_\theta = 0) \times \exp(-10\sqrt{\lambda_{\theta_t}}), \quad \text{for } \lambda_{\theta_t} > 0, \tag{19}$$

and where q_t denotes the free-stream turbulence.

The spot-propagation rate and the spot spreading half-angle asymptotically approach a maximum value for high negative values of λ_θ, but n is allowed to increase to infinity for high negative values of λ_{θ_t}, where λ_{θ_t} is the pressure gradient at the transition onset location, x_t. The value of the intermittency parameter, $\gamma(x)$, is zero for $x \leq x_t$, and increases downstream from the transition point, asymptotically to a maximum value of unity, which corresponds to fully turbulent flow. An effective eddy-viscosity for the transitional region is obtained by scaling the turbulent eddy-viscosity computed by $\gamma(x)$, i.e., $\mu_{\mathrm{trans}} = \gamma(x)\mu_{\mathrm{turb}}$.

Sanz & Platzer (1998) have used the Gostelow model, originally developed for attached flow, for the prediction of laminar separation bubbles by using the spot-generation rate as a second adjustable parameter along with the location of transition onset. They investigated the influence of the spot-generation rate on the separation bubble by either limiting the breakdown-rate parameter to 1·0, which forces instantaneous transition, or by assuming the value for a zero pressure-gradient. In the present study, a break-down-rate parameter of 1·0 was chosen and the transition onset was either predicted by the Michel criterion (Cebeci & Bradshaw 1977) or by specification as an input parameter.

4. RESULTS AND DISCUSSION

All steady-state and unsteady computations for the NLR 7301 airfoil were performed on a C-type Navier–Stokes grid with 221×91 grid points. The initial wall spacing used was 8×10^{-6} resulting in a $y^+ < 2$ for the chosen Mach number of 0·3 and the Reynolds number of 4×10^6. A total of 40 grid points were used in the wake and the farfield boundary extended 20 chord lengths from the surface. The grid is shown in Figure 1.

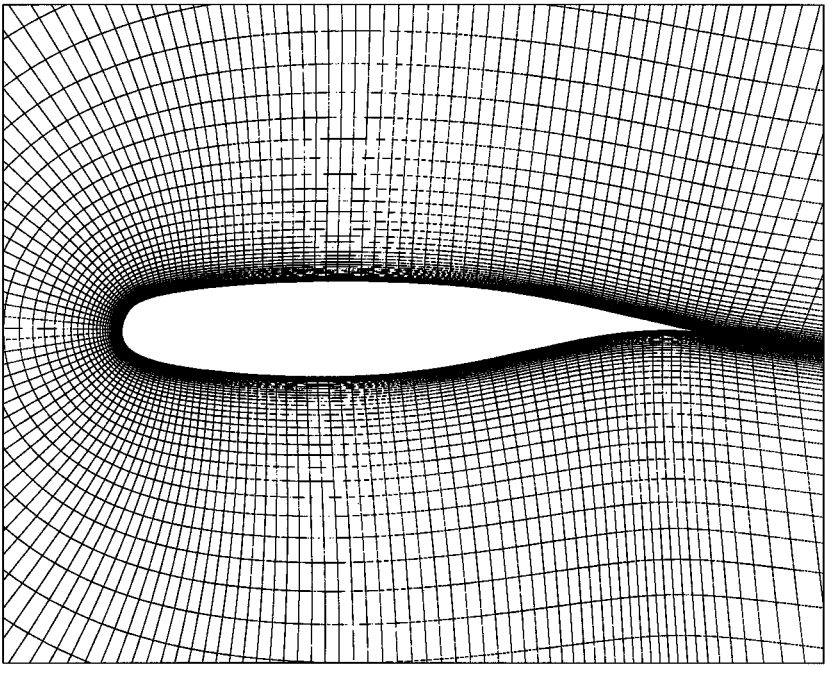

Figure 1. Navier–Stokes C-type grid (221 x 91) for the NLR 7301 airfoil.

A detailed set of measurements for the steady flow at different angles of attack, Mach numbers up to 0·3 and Reynolds numbers up to 4×10^6 have been performed at the NASA Ames Research Center by McCroskey *et al.* (1982). They investigated the static and dynamic characteristics of seven helicopter blades and a supercritical fixed wing airfoil. The supercritical airfoil was chosen for the present study because it is and will be experimentally investigated at the DLR Goettingen to determine its dynamic stall behavior.

4.1. Fully Turbulent Steady-State Computations

The steady-state computations as well as the measurements were obtained at fixed angles of attack in a range from -5° up to 20°. The Mach number for the experiments was approximately 0·3 and the Reynolds number 4×10^6. In Figure 2 the computed steady-state results are compared with the measured data.

Figure 2 shows the linear results obtained with the potential flow panel code UPOT (Teng 1987) and results for viscous computations using the Baldwin–Lomax (BL) and the Baldwin–Barth (BB) turbulence model. All viscous computations were performed assuming fully turbulent flow. The BL- and BB-computed lift coefficients are in close agreement with the measured data for a range of the angle of attack of -5 to 8°. Although the BL- and BB-computed lift coefficients are almost the same up to $\alpha = 8^\circ$, simulations with BB show more flow separation near the trailing edge on the upper surface than BL. For both models this separation grows significantly with increasing angle of attack but the flow stays attached longer for flow simulations with BL due to BL computing higher viscosity. The locations of the separation onset s/c versus the angle of attack for both turbulence models can be seen in Figure 3. Once the flow is separated, it does not reattach. For flow angles of 0 and 5° both turbulence models show no separation. Steady-state solutions in terms of the pressure coefficient distributions versus the chord for $\alpha = 14$, 17 and $17{\cdot}6^\circ$ are given in

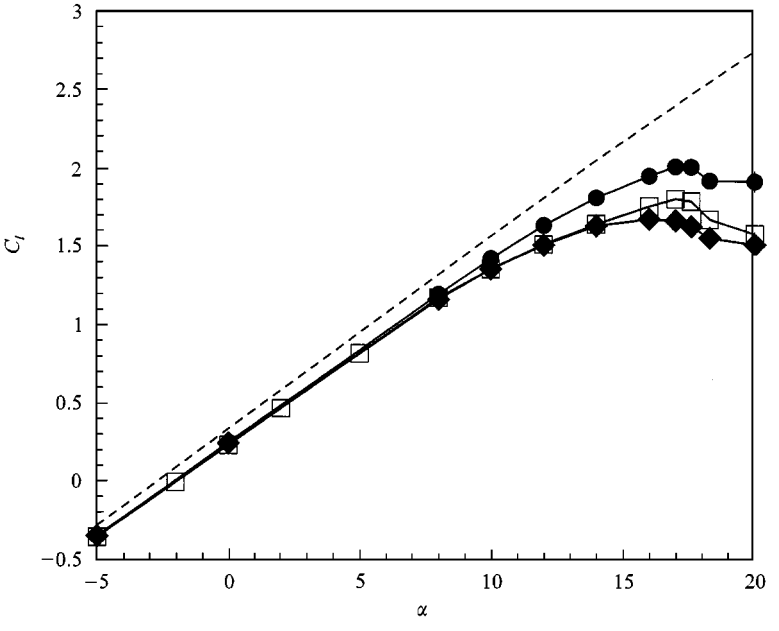

Figure 2. Comparison of the computed and measured lift coefficient: ◆—◆, BB fully turbulent; - - - -, panel code; ●—●, BL fully turbulent; □—□, experimental data by McCroskey *et al.* (1982).

Figures 4–6. These plots show that a higher suction peak is predicted by BL than by BB. Furthermore, the BB model yields a much more constant static pressure in the separation region, as can be seen from the pressure plateaus in front of the trailing edge. Both models predict a nonlinear increase of the lift coefficient for angles of attack higher than 8°. The lift coefficients calculated with the BB model are in good agreement with the measurements up to 14° while the BL model overpredicts the lift for angles of attack in excess of 8° due to the higher suction peak and smaller flow separation.

The BL model predicts the highest lift coefficient at 17° angle of attack in agreement with the experiments, but overpredicts the lift coefficient by 11%. BB predicts the highest lift at an angle of attack of 16°. For angles of attack greater than 14°, the BB model yields a lower lift coefficient than the measurements. It underpredicts the lift by 8%. For angles of attack greater than 17° the convergence behavior of both models is quite different. Although the flow, after reaching the stall angle of approximately 17°, will no longer be steady and therefore the measured and the computed data have to be regarded as averaged values, the BL model converges to a constant lift coefficient up to an angle of attack of 17·6°. In Figure 6 the BL- and BB-computed pressure distributions are compared with the experimental data.

It can be seen that the BB-computed flow on the pressure side is in slightly better agreement with the experiment. On the suction side, except near the suction peak, the BL computed pressures agree with the experiment up to 70% chord. Further downstream the pressure is too low. The BB computed suction peak almost yields the measured peak, but the pressure coefficient between 10 and 70% chord is underpredicted which explains the underprediction of the lift coefficient (Figure 2). The development of the boundary layer along the airfoil for 17·6° is given in Figure 7. For flow angles exceeding 17·6° the computed lift coefficients are no longer steady. This can be seen in Figure 8 where the BL- and the BB-computed lift histories are plotted for the case of 20° incidence angle. It is shown that the BL-computed lift is periodic but reaches values which are considerably higher than the

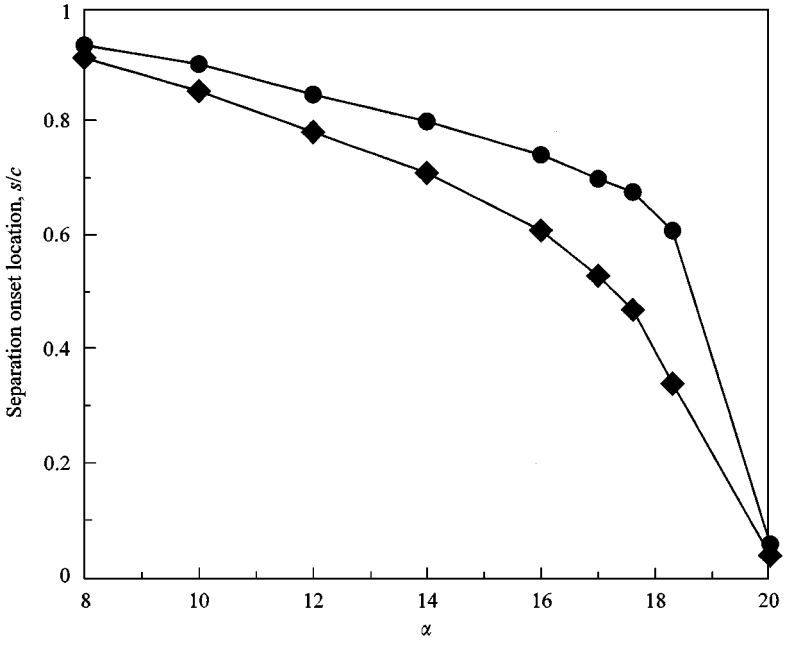

Figure 3. Comparison of the computed separation onset location: ●—●, BL fully turbulent; ◆—◆, BB fully turbulent.

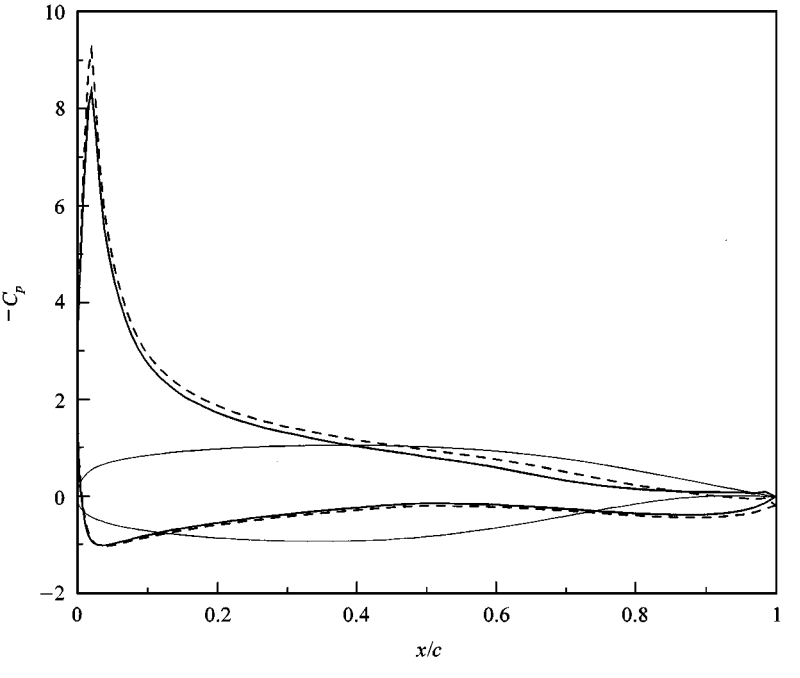

Figure 4. Comparison of the computed pressure coefficient for $\alpha = 14°$: ----, BL fully turbulent; —, BB fully turbulent.

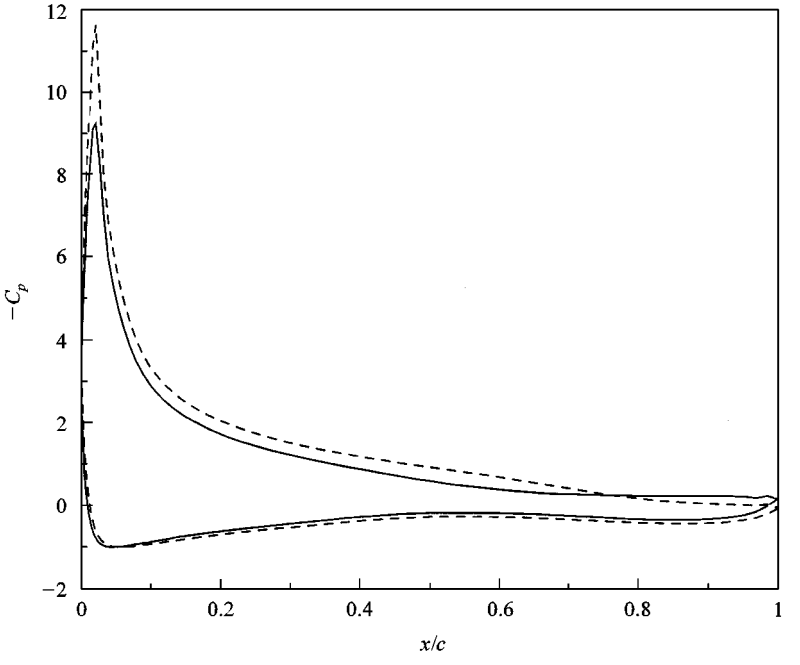

Figure 5. Comparison of the computed pressure coefficient for $\alpha = 17°$: ----, BL fully turbulent; —, BB fully turbulent.

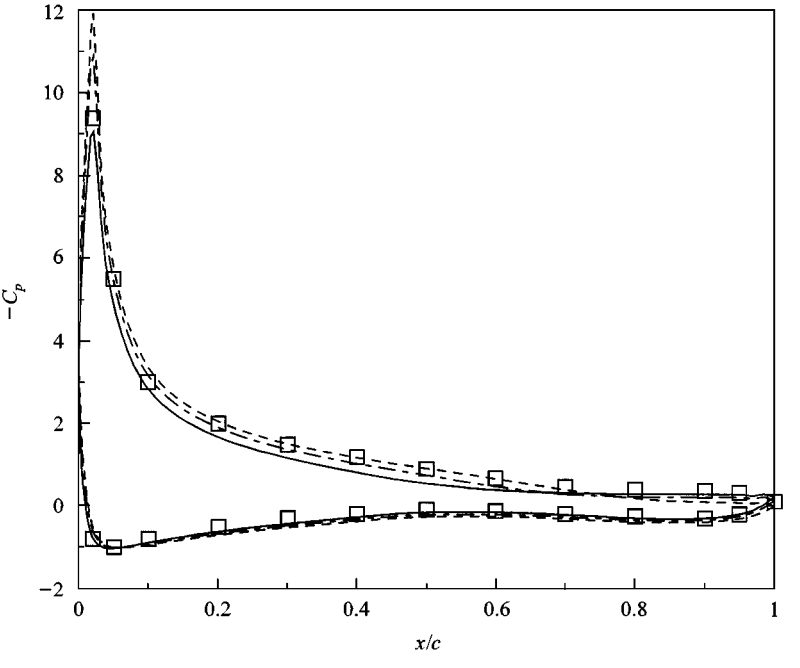

Figure 6. Comparison of the compute and measured pressure coefficient for $\alpha = 17{\cdot}6°$: ----, BL fully turbulent; —, BB fully turbulent; □, experimental data by McCroskey *et al.* (1982); – – – –, BB with transition.

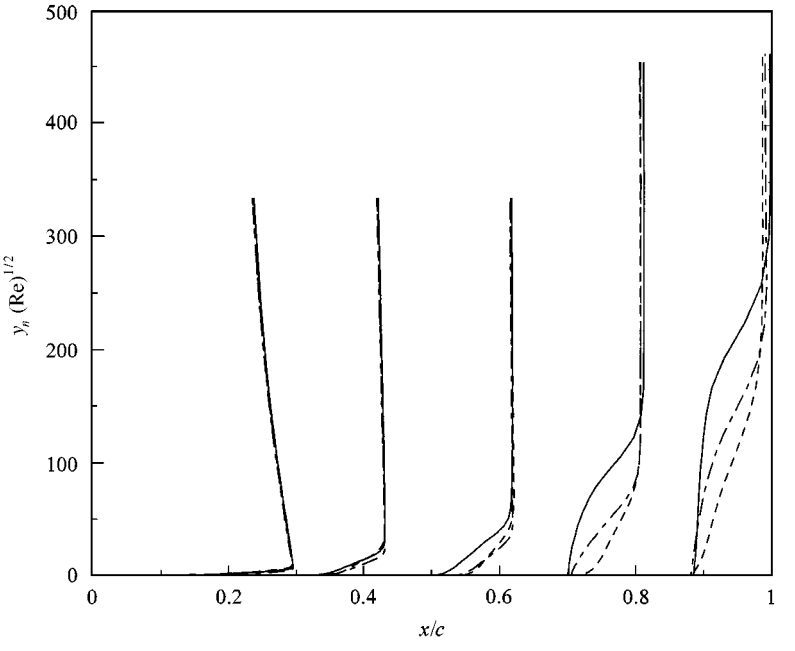

Figure 7. Comparison of the computed boundary layer profiles on the upper surface for $\alpha = 17.6°$: ----, BL fully turbulent; —, BB fully turbulent; – – – –, BB with transition.

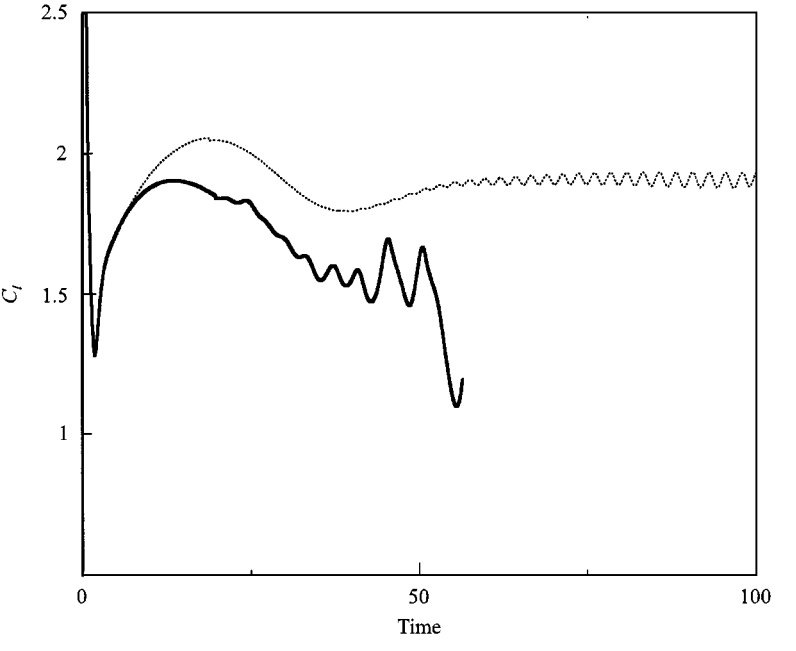

Figure 8. Comparison of the computed time development of the lift coefficient for $\alpha = 20°$: ....., BL fully turbulent; —, BB fully turbulent.

measured value. The BB-computed lift, on the other hand, approaches values considerably closer to the measured value, but then drops dramatically. Figures 9 and 10 depict typical time-instantaneous flow fields computed with the BL and the BB models. The BB model is seen to produce massively separated flow. It should be noted that all the computations were performed time-accurately.

4.2. Steady-State Computations Including Transition

The fully turbulent flow computations described in the previous section show that the BB model is superior to the BL model. However, the sensitivity to transitional flow effects is an important aspect which needs to be studied. Therefore, the computations were repeated with the BB model by assuming that transition starts at $x/c = 0{\cdot}02$ for angles of attack between 14 and $17{\cdot}6^\circ$. The numerical results can be seen in Figure 11.

Figure 11 shows that transition becomes important as the incidence angle is increased. Incorporation of transition substantially improves the agreement with the measured lift values in the high angle of attack range. This improvement can also be seen in Figure 6. On the pressure side, the computations with and without transition differ only slightly, but inclusion of transition yields better agreement with the experimental data on the suction side. Only the suction peak is overpredicted. The development of the boundary layer including transition is given in Figure 7. The separation onset on the suction side was moved downstream from 48% chord without transition to 60% chord with transition.

These numerical results for the NLR 7301 airfoil confirm the findings of Ekaterinaris & Platzer (1996) and Sanz & Platzer (1998) for the NACA 0012 and the Sikorsky SC 1095 airfoils which showed that the numerical prediction of the stall onset is significantly improved by the incorporation of boundary layer transition.

4.3. Dynamic Stall Computations

Unsteady computations were performed for the NLR 7301 airfoil oscillating in the pitching mode described by the equation $\alpha(t) = \alpha_0 + \alpha_1 \sin \omega t$. As in the experiment, the pitch axis was located at the quarter chord point. Two test cases were considered and compared with the unsteady experimental data.

The first test case had a mean angle of $\alpha_0 = 11{\cdot}96^\circ$ and an amplitude of $\alpha_1 = 2{\cdot}0^\circ$. The reduced frequency was $k = 0{\cdot}4$, the Mach number 0·293 and the Reynolds number $3{\cdot}72 \times 10^6$. All unsteady numerical computations were performed time-accurately after calculating a steady-state solution for the mean angle. The unsteady solutions were assumed to be converged if consecutive hysteresis loops did not change. The computations were converged after 3–4 periods.

The experiment was performed with free transition. Figure 12 shows the computed hysteresis loops using the BL model with and without transition. The prediction of the unsteady onset location of transition was obtained with the Michel criterion. It is apparent that the BL model fails to predict the measured hysteresis loop. Repeating the calculations with the BB model, with and without transition, yields much better agreement with the measured hysteresis loop, (Figure 13). Because the unsteady onset locations of transition were not measured, the Michel criterion was used for the calculations.

Additionally, the BB-computed unsteady pressure coefficient distributions on the suction side including transition are compared with the measured pressure distributions in Figure 14 for 20 different angles of attack during the oscillation of the airfoil. It is seen that the computed pressure distributions agree well with the measured distributions.

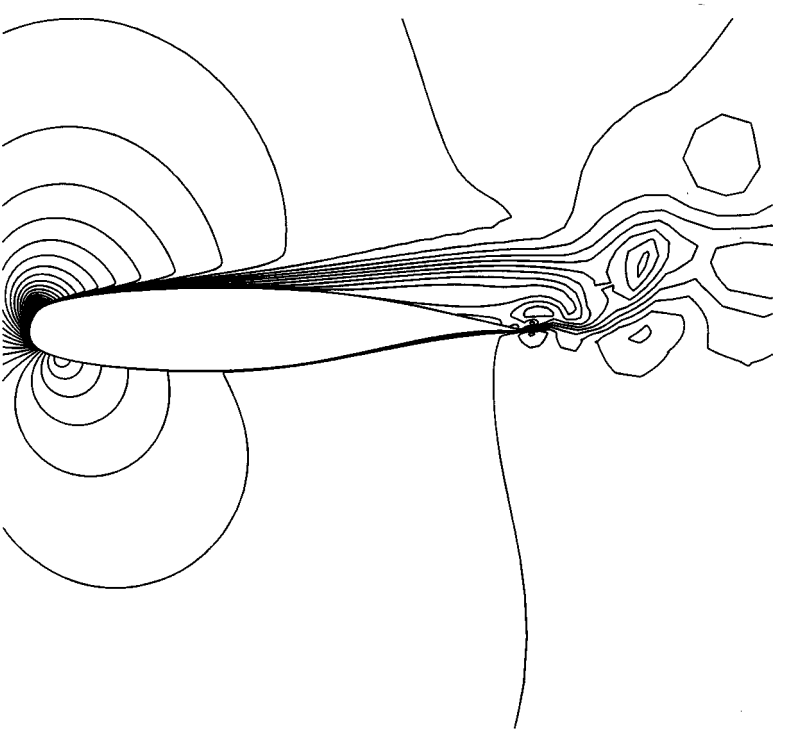

Figure 9. Baldwin–Lomax computed instantaneous Mach number distribution for $\alpha = 20°$.

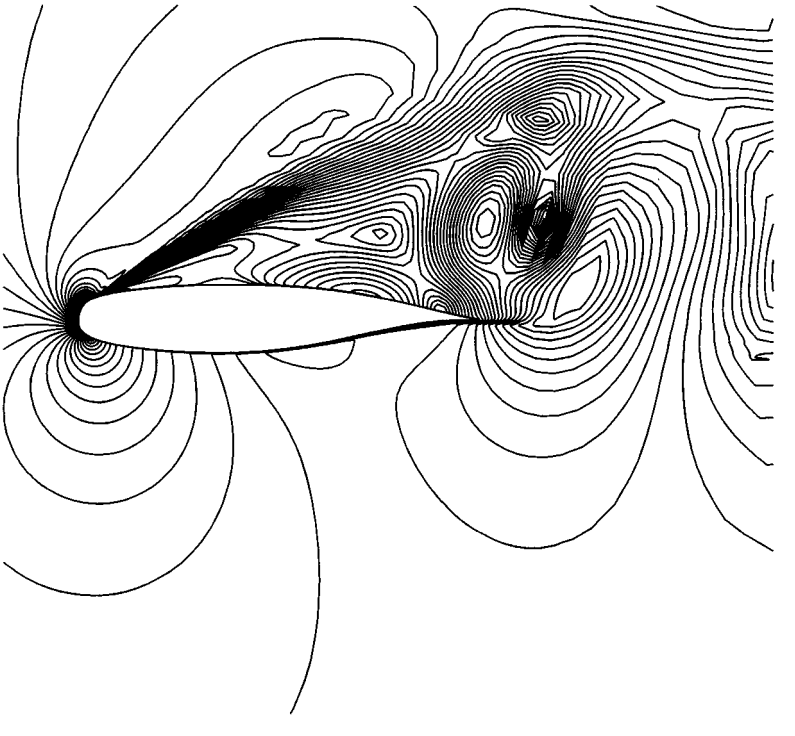

Figure 10. Baldwin–Barth computed instantaneous Mach number distribution for $\alpha = 20°$.

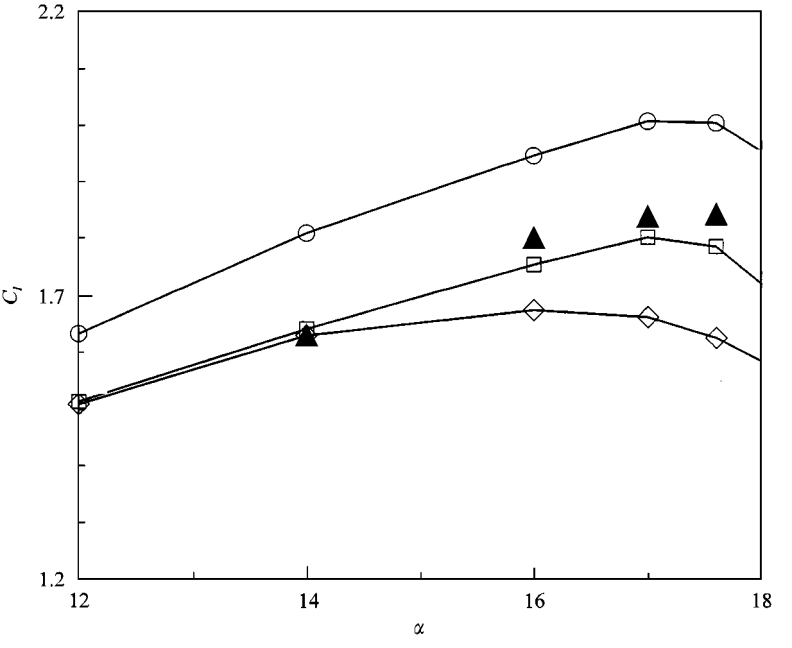

Figure 11. Comparison of the computed and measured lift coefficient with experimental data by McCroskey *et al.* (1982): ◇—◇, BB fully turbulent; ▲, BB with transition; □—□, experimental data; ○—○, BL fully turbulent.

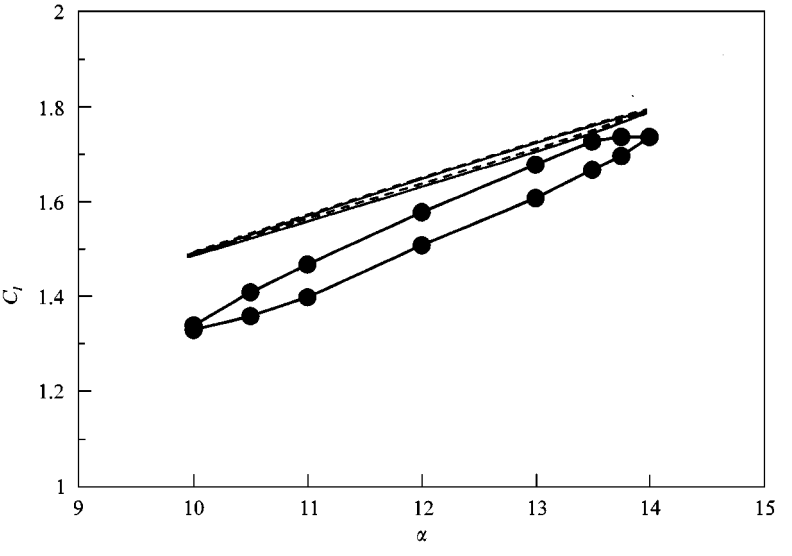

Figure 12. Comparison of the computed and measured unsteady lift coefficient for $\alpha(t) = 11{\cdot}96^\circ + 2{\cdot}0^\circ \sin \omega t$: ●—●, unsteady experimental data by McCroskey *et al.* (1982); —, BL fully turbulent; - - - -, BL with transition.

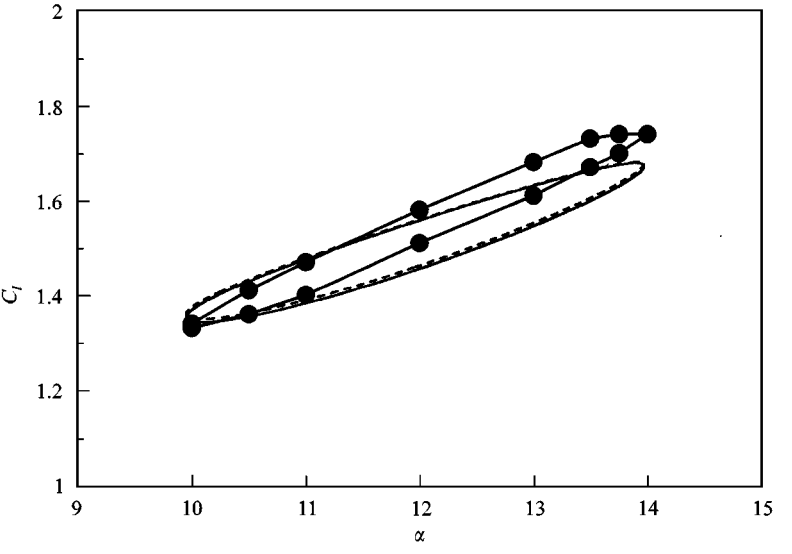

Figure 13. Comparison of the computed and measured unsteady lift coefficient for $\alpha(t) = 11{\cdot}96^\circ + 2{\cdot}0^\circ \sin \omega t$ data by McCroskey *et al.* (1982): ●—●, unsteady experimental data by McCroskey *et al.* (1982); —, BB fully turbulent; ----, BB with transition.

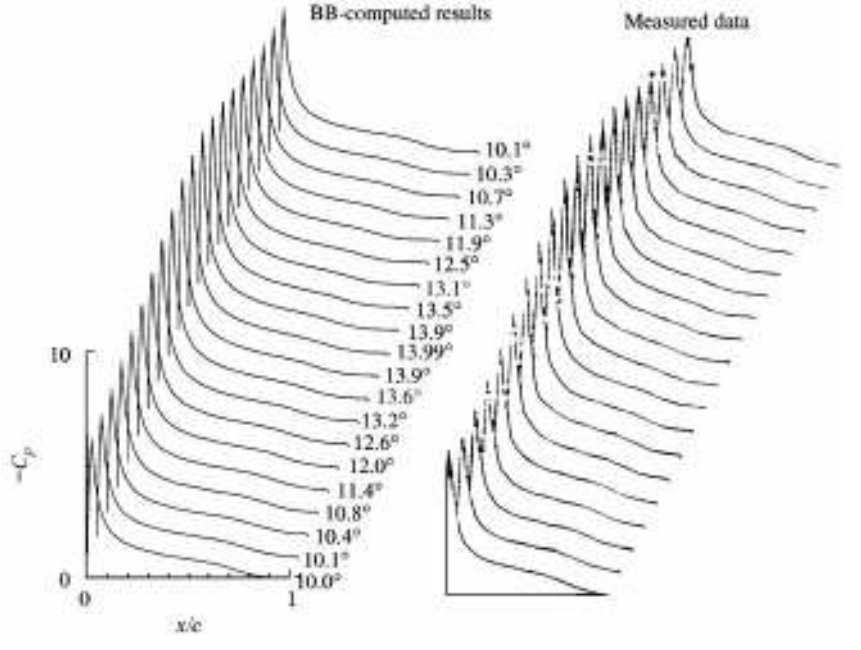

Figure 14. Comparison of the computed and measured unsteady pressure coefficient for $\alpha(t) = 11{\cdot}96^\circ + 2{\cdot}0^\circ \sin \omega t$ including transition with experimental data by McCroskey *et al.* (1982).

From the stability point of view, one is interested whether the oscillation will be damped or excited. This test configuration resulted in a damped oscillation which can be seen from the moment coefficient versus the angle of attack distribution running counter clockwise. The numerical results including transition in comparison with the measured data are given in Figure 15. Both turbulence models predicted a damped oscillation and again the BB result is in much better agreement with the experiment then the BL result.

A second series of computations was performed for the case $\alpha_0 = 9{\cdot}98^\circ$ and $\alpha_1 = 4{\cdot}9^\circ$. The reduced frequency was $k = 0{\cdot}098$, the Mach number 0·299 and the Reynolds number $3{\cdot}79 \times 10^6$. In Figures 16 and 17 one can see the numerically predicted lift coefficient distributions including transition for both turbulence models in comparison with the experimental data. The unsteady onset locations of transition for both calculations were predicted with Michel's criterion because of the unavailability of relevant experimental

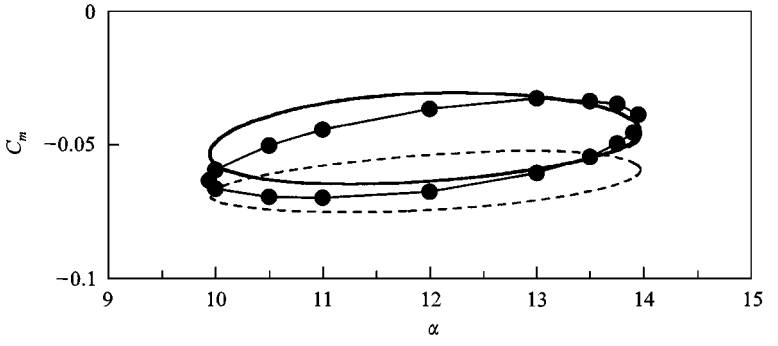

Figure 15. Comparison of the computed and measured unsteady moment coefficient for $\alpha(t) = 11{\cdot}96^\circ + 2{\cdot}0^\circ \sin \omega t$ including transition: ●—●, unsteady experimental data by McCroskey *et al.* (1982); ----, unsteady BL with transition; —, unsteady BB with transition.

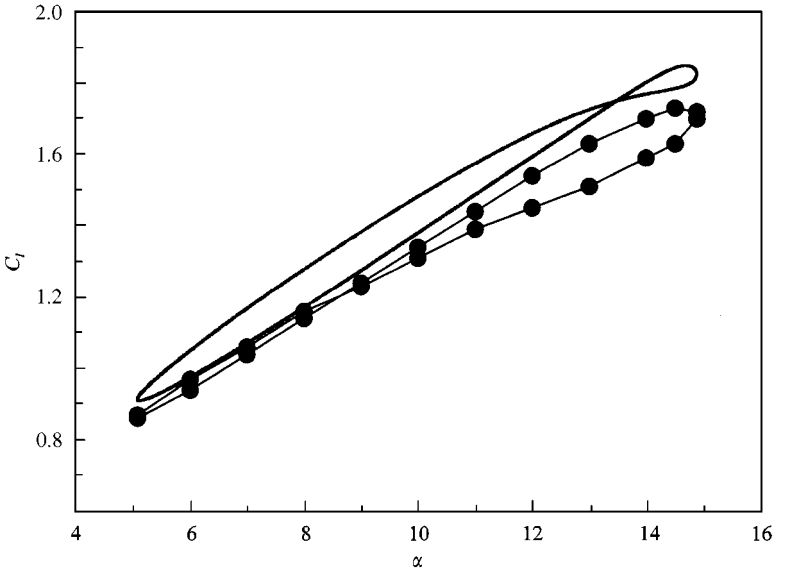

Figure 16. Comparison of the computed and measured unsteady lift coefficient for $\alpha(t) = 9{\cdot}98^\circ + 4{\cdot}9^\circ \sin \omega t$: ●—●, unsteady experimental data by McCroskey *et al.* (1982); — unsteady BL with transition.

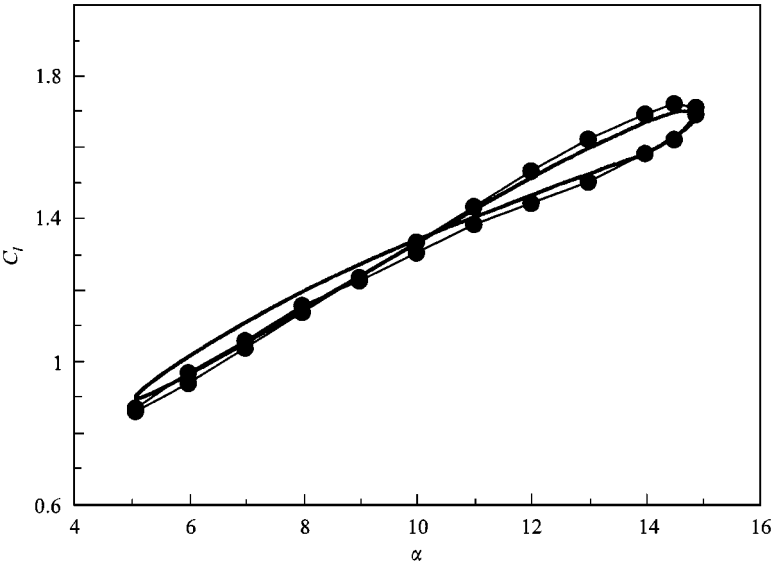

Figure 17. Comparison of the computed and measured unsteady lift coefficient for $\alpha(t) = 9{\cdot}98^\circ + 4{\cdot}9^\circ \sin \omega t$: ●—●, unsteady experimental data by McCroskey *et al.* (1982); — unsteady BB with transition.

transition data. Again, the BB model predicts the measured hysteresis loop much better than the BL model. This is confirmed by the comparison of the computed and measured pressure distributions shown in Figure 18. The experimental data plotted in Figures 16–19 were obtained with free transition. The corresponding moment coefficient distribution in comparison with the experimental data are shown in Figure 19. The oscillation in the second test case investigated was found to be damped in the experiment which was predicted by both turbulence models. All loops of Figure 19 are counter clockwise. In contrast, to the computed lift coefficient distributions, the prediction of the moment coefficient distribution with the BB model is not better then the prediction with the BL model. Both models failed to compute the experimental loop which, as can be seen by the small integrated area of the measured loop, was close to an unstable oscillation.

Dramatically different hysteresis loops were measured if transition was forced. This is shown in Figures 20 and 21. Unfortunately, no information is available on the precise location of the transition strip. The computations assuming fully turbulent flow are shown in Figures 18, 20 and 21. As the fully turbulent approach did not predict the measured lift during the downstroke, it therefore failed to produce an unstable oscillation. In Figure 21 the right part of the experimental hysteresis is clockwise during the downstroke of the airfoil while the BB-computed loop is counterclockwise during the whole oscillation. Clearly, the inclusion of transition has a negligible influence if transition onset is predicted from Michel's criterion.

Therefore, it is not surprising that such a computation fails to reproduce the experimental loop of Figures 20 and 21. It is apparent from the measured pressure distributions shown in Figure 22 that severe flow separation occurs at the start of the downstroke. One would expect that this flow behavior is caused by the sudden burst of a laminar separation bubble. Van Dyken *et al.* (1996) were able to compute the formation and bursting of the bubble on a NACA 0012 airfoil. Therefore, a computation was performed varying the transition onset

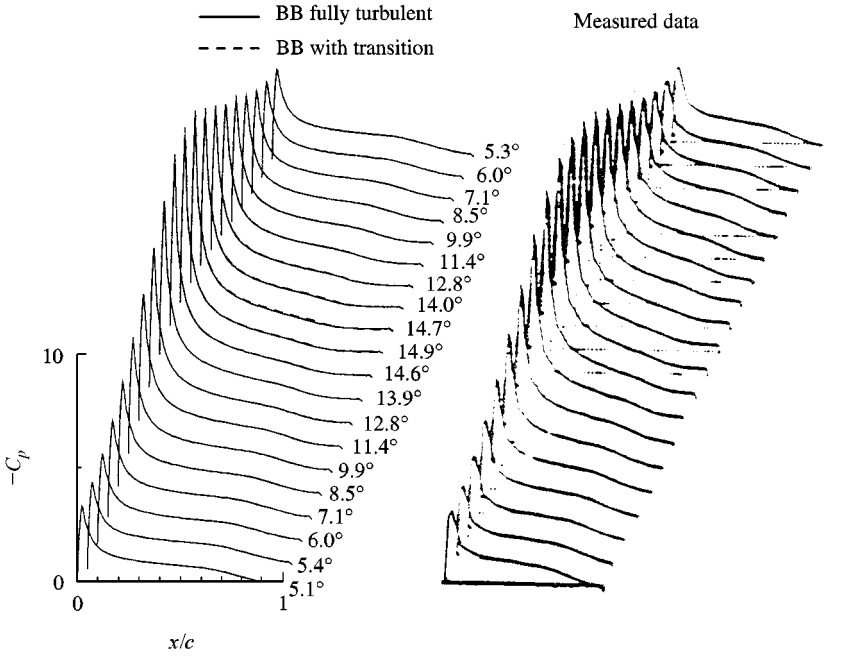

Figure 18. Comparison of the computed and measured unsteady pressure coefficient for $\alpha(t) = 9{\cdot}98^\circ + 4{\cdot}9^\circ \sin \omega t$; experimental data by McCroskey *et al.* (1982).

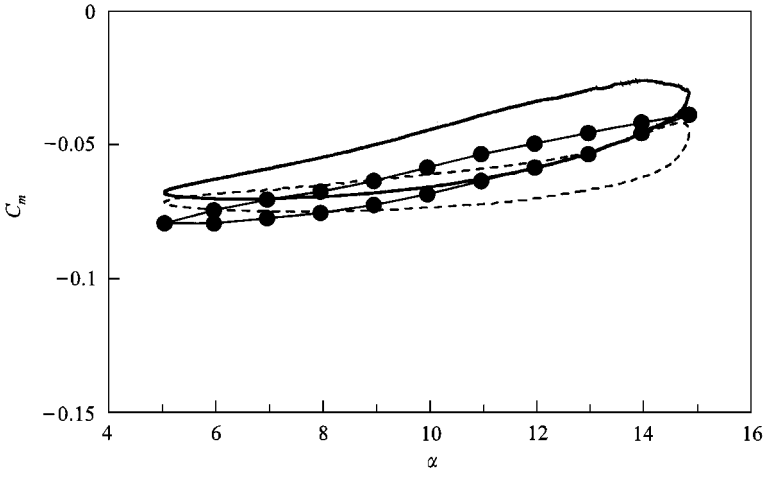

Figure 19. Comparison of the computed and measured unsteady moment coefficient for $\alpha(t) = 9{\cdot}98^\circ + 4{\cdot}9 \sin \omega t$ including transition: ●—●, unsteady experimental data by McCroskey *et al.* (1982); ----, unsteady BL with transition; —, unsteady BB with transition.

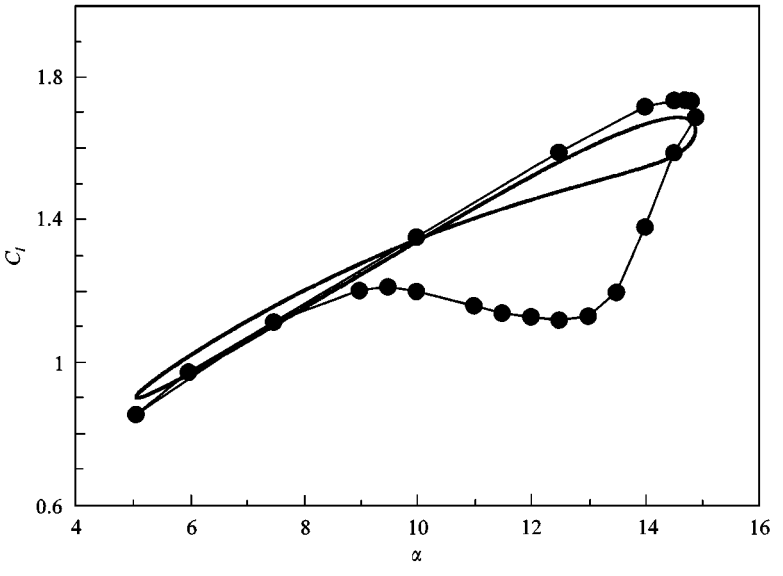

Figure 20. Comparison of the computed and measured unsteady lift coefficient for $\alpha(t) = 9{\cdot}98^\circ + 4{\cdot}9^\circ \sin \omega t$: ●—●, unsteady experimental data by McCroskey *et al.* (1982); —, unsteady BB fully turbulent.

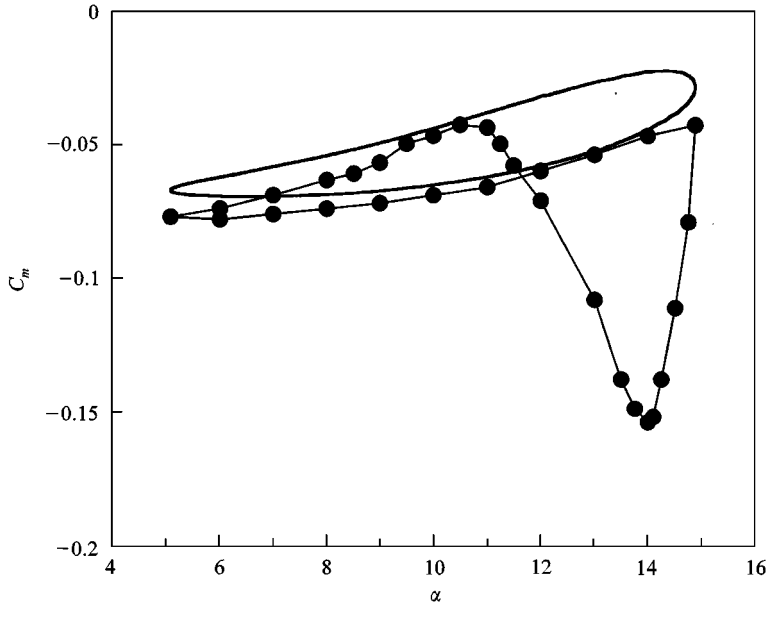

Figure 21. Comparison of the computed and measured unsteady moment coefficient for $\alpha(t) = 9{\cdot}98^\circ + 4{\cdot}9^\circ \sin \omega t$: ●—●, unsteady experimental data by McCroskey *et al.* (1982); — unsteady BB fully turbulent.

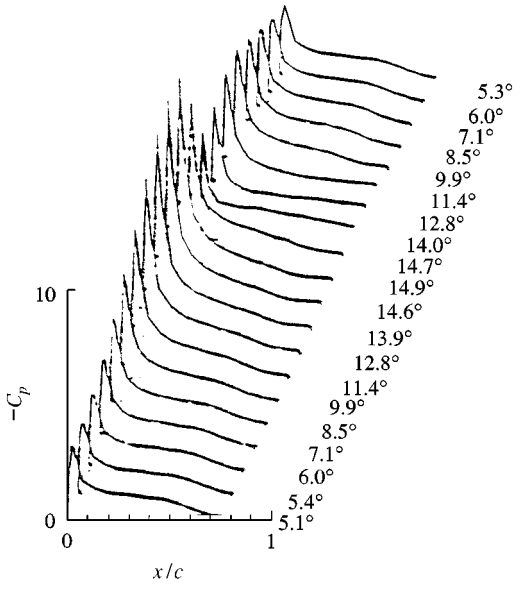

Figure 22. Measured unsteady pressure coefficient for $\alpha(t) = 9{\cdot}98^\circ + 4{\cdot}9^\circ \sin \omega t$; experimental data by McCroskey *et al.* (1982).

location periodically such that the mean position was at $x/c = 0{\cdot}02$ and the amplitude was 1% of the mean position.

However, this simple attempt to model the flow physics was unsuccessful. Clearly, a more detailed analysis is necessary to clarify the flow mechanism which produces the measured loop.

The average computational effort on steady and unsteady calculations can be summarized as follows. The steady-state computations were performed on SGI Octane workstations. Typical steady-state time-accurate computations using the Baldwin–Barth turbulence model including transition needed between 10 000 and 25 000 time steps in the stall region. The time-accurate unsteady computations were run on a C-90 and a T-932 where between 10 000 and 20 000 time steps per cycle with 3 Newton subiterations for every time step were necessary.

5. CONCLUSIONS

A 2-D thin-layer Navier–Stokes code was used in conjunction with the Baldwin-Lomax and Baldwin–Barth turbulence models to predict the steady and dynamic stall behavior of the supercritical NLR 7301 airfoil. The influence of transition was investigated by the incorporation of the transition model of Gostelow *et al.*

The BB model was found to give consistently better agreement with the experimental data than the BL model except for the predicted moment coefficient loop for the second test case (Figure 19). Furthermore, the incorporation of boundary layer transition yielded additional improvements, especially for the steady-state analysis, provided that the "correct" transition onset location was chosen. Further work is clearly needed to develop reliable criteria for transition onset under unsteady adverse pressure gradient conditions.

Ultimately, the computations need to be extended to account for 3-D effects based on the full Navier–Stokes equations.

ACKNOWLEDGEMENTS

The first author gratefully acknowledges the support of the Deutsche Forschungsgemeinschaft (DFG) for the Post-Doctoral Research stay and the Naval Postgraduate School. Also, the authors are indebted to Dr J. Ekaterinaris, Senior Research Scientist at NIELSEN Engineering and Research Inc., Dr W. Sanz at the Technical University Graz, Austria, and Dr K. Jones at the Naval Postgraduate School for their advice. NAVO provided computing time on the DoD High Performance Computing Systems.

References

Baldwin, B. S. & Lomax, H. 1978 Thin layer approximation and algebraic model for separated turbulent flow. AIAA Paper 78–257.

Baldwin, B. S. & Barth, T. J. 1990 A One-equation turbulence transport model for high Reynolds number wall-bounded flows. NASA TM 102847.

Carr, L. W. & Chandrasekhara, M. S. 1996 Computational prediction of airfoil dynamic stall. *Progress in Aerospace Sciences* **32,** 523–573.

Cebeci, T. & Bradshaw, P. 1977 *Momentum Transfer in Boundary Layers*. Washington: Hemisphere Publishing Corporation, p. 153.

Chakravarthy, S. R. & Osher, S. 1985 A new class of high accuracy TVD schemes for hyperbolic conservation laws. AIAA Paper 85–0363.

Clarkson, J. D., Ekaterinaris, J. A. & Platzer, M. F. 1993 Computational investigation of airfoil stall flutter. *Proceedings International Symposium on Unsteady Aerodynamics, Aeroacoustics and Aeroelasticity of Turbomachines and Propellers* pp. 415–432. Berlin: Springer Verlag.

Ekaterinaris, J. A. & Platzer, M. F. 1997 Computational prediction of the airfoil dynamic stall. *Progress in Aerospace Sciences* **33,** 759–846.

Ekaterinaris, J. A. & Platzer, M. F. 1996 Numerical investigation of stall flutter. *ASME Journal of Turbomachinery* **118,** 197–203.

Ekaterinaris, J. A., Chandrasekhara, M. S. & Platzer, M. F. 1995 Analysis of low Reynolds number airfoil flows. *Journal of Aircraft* **32,** 625–630.

Ekaterinaris, J. A., Cricelli, A. S. & Platzer, M. F. 1994 A zonal method for unsteady viscous compressible airfoil flows. *Journal of Fluids and Structures* **8,** 107–123.

Gostelow, J. P., Melwani, N. & Walker, G. J. 1996 Effects of a streamwise pressure gradient on turbulent spot development. *ASME Journal of Turbomachinery* **118,** 737–747.

Groshmeyer, S. P., Ekaterinaris, J. A. & Platzer, M. F. 1991 Numerical investigation of the effect of leading edge geometry on dynamic stall of airfoils. *AIAA 22nd Fluid Dynamics, Plasma Dynamics Lasers Conference*, AIAA Paper No. 91–1798.

Mccroskey, W. J., Mcalister, K. W., Carr, L. W., Pucci, S. 1982 An experimental study of dynamic stall on advanced airfoil sections. NASA Technical Memorandum 84245, Vols. 1, 2 and 3, USAAVRADCOM TR-82-A-8.

Rai, M. M. & Chakravarthy, S. R. 1988 An implicit form of the Osher upwind scheme. *AIAA Journal* **24,** 735–743.

Sanz, W. & Platzer, M. F. 1998 On the Navier–Stokes calculation of separation bubbles with a new transition model. *ASME Journal of Turbomachinery* **120,** 36–42.

Schewe, G. & Deyhle, H. 1996 Experiments on transonic flutter of a two-dimensional supercritical wing with emphasis on the non-linear-effect. *Proceedings of the Royal Aeronautical Society Conference on Unsteady Aerodynamics*, London, U.K.

Steger, J. L. & Warming, R.F. 1981 Flux vector splitting of the inviscid gas dynamic equations with applications to finite-difference methods. *Journal of Computational Physics* **40,** 263–293.

Teng, N. H. 1987 The development of a computer code for the numerical solution of unsteady, inviscid and incompressible flow over an airfoil. Master's thesis, Naval Postgraduate School, Monterey, CA, U.S.A.

Van Dyken, R. D., Ekaterinaris, J. A., Chandrasekhara, M. S., Platzer, M. F. 1996 Analysis of compressible light dynamic stall flow at transitional Reynolds numbers. *AIAA Journal* **34,** 1420–1427.

APPENDIX: NOMENCLATURE

a_∞	free-stream speed of sound
c	chord length
C_l	lift coefficient
C_p	pressure coefficient
e	total energy per unit volume
f	frequency in Hz
k	reduced frequency, $2\pi fc/U_\infty$
M_∞	free-stream Mach number
Re	Reynolds number, cU/v
t	nondimensional time, $\hat{t}a_\infty/c$
U	local free-stream velocity
U_∞	free-stream velocity magnitude
u, v	velocity components
x	coordinate parallel to chord
x_t	transition onset location
y^+	nondimensional normal wall distance
θ	boundary layer momentum thickness
κ	ratio of specific heats
μ	viscosity
v	kinematic viscosity
v_t	turbulent viscosity
ρ	density
ρ_∞	free-stream density
$\dot{(\,)}$	differentiation with respect to t
$\vert_{\text{wall}}$	quantity on the surface of the blade